

Spatial Collection in Colloidal Quantum Dot Solar Cells

Olivier Ouellette, Antoine Lesage-Landry, Benjamin Scheffel, Sjoerd Hoogland,
F. Pelayo García de Arquer, and Edward H. Sargent*

In thin-film photovoltaic (PV) research and development, it is of interest to determine where the chief losses are occurring within the active layer. Herein, a method is developed and presented by which the spatial distribution of charge collection, *operando*, is ascertained, and its application in colloidal quantum dot (CQD) solar cells is demonstrated at a wide range of relevant bias conditions. A systematic computational method that relies only on knowledge of measured optical parameters and bias-dependent external quantum efficiency spectra is implemented. It is found that, in CQD PV devices, the region near the thiol-treated hole-transport layer suffers from low collection efficiency, as a result of bad band alignment at this interface. The active layer is not fully depleted at short-circuit conditions, and this accounts for the limited short-circuit current of these CQD solar cells. The high collection efficiency outside of the depleted region agrees with a diffusion length on the order of hundreds of nanometers. The method provides a quantitative tool to study the operating principles and the physical origins of losses in CQD solar cells, and can be deployed in thin-film solar cell device architectures based on perovskites, organics, CQDs, and combinations of these materials.

Thin-film materials ranging from organics to colloidal quantum dots (CQDs) to perovskites have attracted intensive recent interest in photovoltaics (PVs). In thin-film photovoltaic research and development, it is of interest to determine where the chief losses are occurring within the active layer. We developed, and present herein, a method by which we ascertain the spatial distribution of charge collection, *operando*, and demonstrate its application in CQD solar cells at a wide range of relevant bias conditions. We implement a systematic computational method that relies only on knowledge of measured optical parameters and bias-dependent external quantum efficiency (EQE) spectra. We use an experimentally derived Gaussian-noise regularized least-squares approach to determine the spatial profile of the efficiency with which photocarriers are collected in such devices. We find that, in CQD PV devices, the region near the thiol-treated hole-transport layer (HTL) suffers

from low collection efficiency, as a result of bad band alignment at this interface. The active layer is not fully depleted at short-circuit conditions, and this accounts for the limited short-circuit current of these CQD solar cells. The high collection efficiency outside of the depleted region agrees with a diffusion length on the order of hundreds of nanometers. The method provides a quantitative tool to study the operating principles and the physical origins of losses in CQD solar cells, and can be deployed in thin-film solar cell device architectures based on perovskites, organics, CQDs, and combinations of these materials.

CQDs have been studied as photovoltaic materials for their promise in contributing to affordable solar electricity,^[1–3] with record power conversion efficiencies (PCEs) now exceeding 13%.^[4] Recent advances in structural and energetic ordering in CQD solids have brought the certified efficiency of CQD solar cells to exceed 12%.^[5]

Despite these recent strides in performance, there remains room to improve CQD solar cells in short circuit current (J_{SC}), fill factor (FF), and open-circuit voltage (V_{OC}).^[6] Understanding of the origins of present-day limits to performance has progressed thanks to research focused on the energetic distribution of imperfections—bandedge and trap states.^[7–11] Some losses have been ascribed to specific regions and interfaces within the active layer;^[12–14] however, the spatial distribution of these imperfections and their impact on performance has yet to be measured in CQD solar cells *operando*.

Evaluating the spatial collection efficiency (SCE), i.e., the yield with which locally photogenerated charge carriers contribute to the photocurrent, has been used to study other types of photovoltaic devices such as crystalline Si,^[15–17] GaAs,^[17] CdS/CdTe,^[15,17] CIGS,^[18] as well as photoelectrochemical cells.^[16] Extending this characterization tool to new device architectures, such as CQD, perovskite, and organic solar cells, remains a challenge due to the complex effect of thin-film interference, for this effect precludes the use of conventional analytical methods^[15,17,19] in the calculation of the SCE. Rekemeyer et al. have made significant progress toward experimentally obtaining the SCE in a CQD device;^[20] however, they did so using electron-beam induced current (EBIC) analysis in a scanning electron microscope (SEM), an *ex situ*, destructive method requiring high vacuum and which relies on an electron beam rather than light for carrier excitation,^[21] while ZnO requires

Dr. O. Ouellette, Dr. A. Lesage-Landry, B. Scheffel, Dr. S. Hoogland,
Dr. F. P. García de Arquer, Prof. E. H. Sargent
Department of Electrical and Computer Engineering
University of Toronto
10 King's College Road, Toronto, Ontario M5S 3G4, Canada
E-mail: ted.sargent@utoronto.ca

 The ORCID identification number(s) for the author(s) of this article can be found under <https://doi.org/10.1002/adfm.201908200>.

DOI: 10.1002/adfm.201908200

UV irradiation to reach the doping and conductivity necessary for device operation.^[22]

In this work, we report a nondestructive method to obtain the bias-dependent SCE of thin-film solar cells and apply it to CQD solar cells under operating conditions. We first present the corresponding ill-posed, ill-conditioned inverse problem and our numerical approach to solving it using Gaussian-noise regularization. We then use the method to calculate the SCE in CQD solar cells. We show that collection efficiency is the highest for charge carriers generated near the front of the active layer and in the hole-transport layer, which is indicative of higher carrier depletion in these regions. We observe that the region near the hole-transporting QD layers suffers from low collection efficiency, suggesting a suboptimal band alignment at this interface. We find ultimately that losses in J_{SC} are almost equally apportioned between carrier extraction and optics, indicating that CQD solar cells will benefit from advances in both light management and material quality.

1. Calculating the Collection Efficiency

Obtaining the collection efficiency as function of position requires solving the following Fredholm integral equation^[15,18]

$$\eta(\lambda) = \int_0^t G(z, \lambda) \phi(z) dz \quad (1)$$

where $\eta(\lambda)$ is the measured internal quantum efficiency (IQE) spectrum, t is the total thickness of the active layer, $G(z, \lambda)$ is the spectral photogeneration probability profile, and $\phi(z)$ is the SCE. The variables z and λ are the position and wavelength, respectively. In this context, IQE is defined as the ratio of extracted charge carriers to photons absorbed in the active layer. While the IQE can be directly measured using conventional methods,^[23–25] the generation probability must be calculated using the transfer matrix method^[26,27] and normalized in the z -dimension so that a unity extraction efficiency yields a unity IQE. Calculating $G(z, \lambda)$ requires, as an input, the thickness and complex refractive index spectrum of each layer in the device, which can be obtained using spectroscopic ellipsometry.

In optically thick active layers such as in crystalline silicon solar cells, $G(z, \lambda)$ has a simple exponential form and Equation (1) can be solved analytically^[15,19,28] or numerically.^[29] This is, however, not the case for thin-film solar cells, in which thin-film interference plays an important role and causes $G(z, \lambda)$ to deviate significantly from its simple analytical form.^[27] This translates to the presence of peaks and valleys in absorption and EQE spectra that cannot be traced back to features in the absorption coefficient spectrum. These interference effects are enhanced when using an active layer with a low absorption-coefficient-to-thickness ratio and a reflective back-contact, both of which apply to CQD solar cells. With such deviations of $G(z, \lambda)$ from a simple exponential form, solving (1) for $\phi(z)$ becomes an ill-posed, ill-conditioned inverse problem and thus possesses an infinite number of solutions. Within this set of mathematical solutions lies the unique physical solution to the problem.^[16] Advanced numerical methods must be used to retrieve the spatial collection efficiency from Equation (1) in thin-film solar cells.

Because the problem is ill-conditioned, we use regularization to find the stable, non-overfitted, physical solution bounded between 0 and 1. In recent reports, Pang et al. made use of truncated singular-value decomposition,^[18] whereas Segev et al. implemented Tikhonov regularization.^[16] The former method is prone to oscillatory artifacts and may yield unphysical results,^[30] while the latter method requires manually setting a regularization parameter and making assumptions on the properties of the solution ϕ , such as its slope or curvature, which precludes its use for discontinuous active layers (heterojunctions).

We instead use a method where regularization is done through the addition of Gaussian noise to the experimental input data,^[31] allowing for the retrieval of a noise-stable ϕ . Furthermore, setting the noise to correspond to the measurement noise removes the need to resort to free parameters. We convert Equation (1) to the following discretized, regularized, convex program

$$\phi = \arg \min_{\phi \in [0,1]^m} \|\bar{G}\phi - \bar{\eta}\|_2^2 \quad (2)$$

with ϕ the resulting SCE, \bar{G} the Gaussian-noise perturbed photogeneration matrix, and $\bar{\eta}$, the Gaussian-noise perturbed IQE. The method is detailed in full in Section S1 in the Supporting Information.

2. Experimental Measurements

CQD solar cells were fabricated following the procedure of ref. [32], with their structure shown in **Figure 1a**. On the illuminated side, an n-type ZnO layer serves as an electron-transport layer (ETL). The active layer is composed of PbS CQDs treated with lead halides (PbI₂ and PbBr₂, PbX₂ hereafter), with their exciton peak located at 1.33 eV. At the rear, CQDs with a slightly higher bandgap are used (1.46 eV) and are treated with ethanedithiol (EDT) to facilitate hole extraction and effectively constitute an HTL^[13] (see the Experimental Section).

We began by measuring, using spectroscopic ellipsometry, the complex refractive index spectrum of each layer deposited individually on a glass substrate (**Figure 1b**; **Figures S1–S5**, Supporting Information). The thickness of each layer in the complete device was evaluated using SEM imaging (**Figure 1a**).

With the refractive indices and thicknesses in hand, we proceeded to calculate the light intensity distribution within the device using the transfer matrix formalism.^[27] The resulting spectral generation probability profile $G(z, \lambda)$ in the CQD active layer is shown in **Figure 1d**, along with the corresponding absorption spectrum in **Figure 1c** and photogeneration rate under AM1.5G illumination in **Figure 1e**. Optimizing the input parameters is required to reach good agreement between the calculated absorptance and the -2 V biased EQE spectrum (see **Figures S6** and **S7** in the Supporting Information), which corresponds to absorption in the active layer—with no contribution from parasitic absorption or reflection in other layers—under the assumption that all photogenerated charge carriers are collected by the applied electric field.^[23] This assumption is valid for pin (or equivalent) architectures such as in CQD solar cells, since the active layer can be fully depleted using an applied

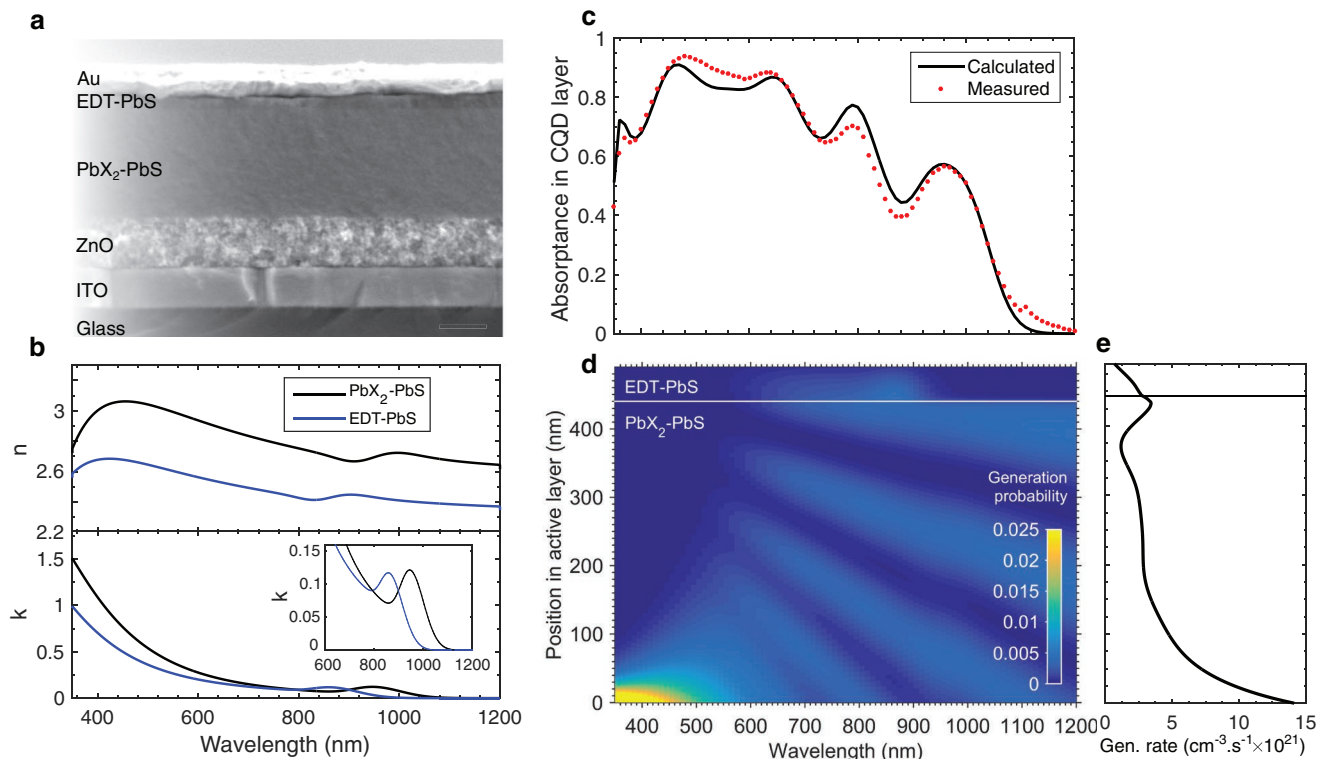


Figure 1. Acquiring $\mathbf{G}(z, \lambda)$: optical modeling of CQD solar cells. a) SEM image showing the architecture of the device, with ITO as the front contact, ZnO nanoparticles as the ETL, halide-treated CQDs as the active layer, EDT-treated CQDs to promote hole extraction, and gold as the reflective back contact. Scale bar is 200 nm. b) Real (n) and complex (k) part of the refractive index of both components of the active layer, measured with spectroscopic ellipsometry. c) Calculated absorption spectrum in the active layer (line) and measured EQE at a bias of -2 V (points). d) Generation probability matrix $G(z, \lambda)$ from transfer matrix modeling. e) Photogeneration rate profile within the active layer under the AM1.5G illumination spectrum. See also Figures S1–S7 in the Supporting Information.

voltage. For this correspondence, the collected photocurrent must be voltage-independent (i.e., the J – V curve must be flat at reverse-bias). The spatial distribution of the generation rate is given by

$$G_z(z) = \int_0^\infty G(z, \lambda) b_i(\lambda) d\lambda \quad (3)$$

with $b_i(\lambda)$ the incident photon flux—the AM1.5G reference spectrum in this case. $G_z(z)$ (Figure 1e) exhibits the usual Beer–Lambert exponential profile at shorter wavelengths, where the absorption length of CQDs resides below the device thickness; whereas significant constructive- and destructive-interference peaks and valleys appear beyond 600 nm wavelength, yielding small but non-negligible generation near the reflective back contact.

In addition to evaluating \mathbf{G} itself, we evaluated its element-wise experimental error in the form of the variance matrix σ_G^2 via a Monte Carlo method. We did so by performing the transfer matrix calculation K times with modified layer thicknesses for each iteration to obtain modified photogeneration matrices \mathbf{G}_k , for $k = 1, 2, \dots, K$. The thicknesses were pooled from a normal distribution with a mean and variance estimated from thickness measurements performed using an SEM. The element-wise variance of the resulting \mathbf{G}_k matrices constitutes the variance matrix σ_G^2 . Details and values are provided in the Supporting Information.

Next, we characterized the photovoltaic performance of devices in order to obtain the internal quantum efficiency $\eta(\lambda)$. The current density–voltage (J – V) curve in Figure 2a was measured under simulated AM1.5G solar illumination in a nitrogen atmosphere, yielding a PCE of 10.6%. Markers in Figure 2a indicate the bias voltages at which the EQE spectra were taken, also in a N_2 atmosphere (Figure 2b). At forward biases beyond the maximum-power point (MPP) of 0.5 V, the EQE signal-to-noise is significantly reduced and reliable spectra could not be acquired. The J – V curve is flat at negative biases up to -2 V ($R_{\text{shunt}} > 10 \text{ k}\Omega \text{ cm}^2$) indicating that photogenerated carriers are efficiently extracted using the applied electric field, providing a simple way to obtain the maximum photogeneration spectrum, which corresponds to the absorption spectrum in the active layer.^[23,24] The equivalence between reverse-biased EQE and active layer absorbance is only valid in the bias range where photocurrent extraction becomes voltage-independent, which, in pin or similar architectures, implies full depletion of the active layer and carrier transit times much smaller than their excited lifetime.^[33] We have set this voltage point to -2 V, as it is the largest reverse-bias which does not cause diode breakdown, ensuring complete photogenerated-carrier collection. The resulting IQE spectra shown in Figure 2c were calculated directly by dividing the corresponding EQE curves by the -2 V biased EQE, since it is experimentally equivalent to the absorbance in the active layer.

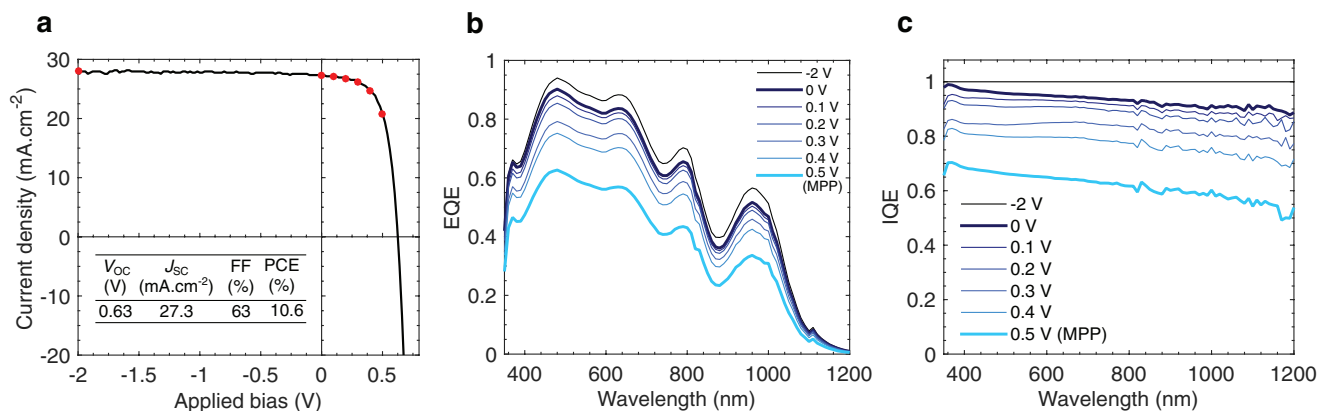


Figure 2. Acquiring $\eta(\lambda)$: photovoltaic characterization of CQD solar cells. a) Current density–voltage (J – V) curve under simulated AM1.5G solar illumination. Markers indicate the bias voltages at which the EQE spectra were measured. b) EQE spectra measured at different bias voltages. c) IQE spectra obtained from (b): $\text{IQE}(V) = \text{EQE}(V)/\text{EQE}(-2\text{ V})$.

3. Discussion of Inner Device Physics

We then used the computed G and experimentally determined η to calculate ϕ using Equation (2) (Figure 3a). We performed a sensitivity analysis and found the estimated error on the results to be within 5% of the reported value (Figure S8, Supporting Information). The IQE spectra (Figure 3b) found by multiplying G and the SCEs ϕ show a good agreement with the experimental data, with mean square errors below 2×10^{-5} . Several observations can be made from the SCE profiles; from these observations, we propose a schematic band diagram (Figure 3c,d) that is consistent with the SCE profiles, as explained below.

First, collection efficiency is high near the ZnO:PbS interface, where most charge carriers are photogenerated, confirming the leading role of this heterojunction in carrier extraction. At 0 V, we also observe that collection efficiency remains above 90% up to 350 nm away from this junction. A near-unity SCE in low-doping materials such as CQD solids is understood to originate from sufficient drift-diffusion transport which drives charge separation and allows photogenerated electrons and holes to reach the electron- and hole-accepting contacts, respectively.^[15] High collection efficiency at this edge of the active layer implies that no energy barrier nor surface states precludes electron extraction; and that holes fully traverse the active layer faster than they can recombine, which suggests advantageous band-bending (Figure 3c) and thus a significant drift component in their driving force. If holes are generated farther from the junction, the distance they must cover is reduced, but so is the band-bending and the corresponding drift component, leading to a slight decrease in SCE. In addition, collection efficiency drops with applied forward-bias, which we ascribe to flattening of the bands (Figure 3d) and a further decrease in drift transport. This could be caused, for example, by insufficient n-type doping in the ZnO ETL, or undesirably high background doping in the PbX_2 –PbS active layer^[34] (Figure S9, Supporting Information).

The importance of the ZnO:PbS interface for carrier extraction is specific to active layer materials with relatively low diffusion lengths, as diffusion transport must be complemented by the drift component enabled by the heterojunction, which thus serves a carrier extraction purpose, in addition to the carrier selectivity provided by its wide valence-band barrier. At MPP,

the collection efficiency does not drop sharply away from the junction, where bands are flat and charge transport is mainly diffusive. A diffusion length that is comparable to the active layer thickness, consistent with recent measurements,^[35] can thus be inferred,^[15] although quantifying it accurately from SCE profiles is challenging in architectures more complex than pn junctions, such as that of CQD solar cells. An increased diffusion length would flatten the SCE in undepleted regions, enabling thicker active layers and higher J_{SC} and FF through improved carrier collection and light absorption.^[5]

Turning to the rear-side of the active layer, we observe that collection is efficient at the EDT–PbS: Au interface, suggesting advantageous band-bending provided by this metal–semiconductor junction, which indicates that the workfunction of EDT–PbS is shallower than that of the Au contact ($\Phi_{\text{EDT}} < \Phi_{\text{Au}}$). Furthermore, at 0 V, the EDT–PbS is depleted over 40 nm away from the metal: this is in line with the near-intrinsic character of the EDT–PbS.^[13] In addition, the depletion width narrows with applied forward-bias, as expected.^[34] This translates to the SCE dropping sharply away from this junction at forward-bias, indicative of low diffusion length for electrons or holes in this region. In addition, the SCE is observed to greatly improve in a 20 nm region directly at the interface, which is caused by the pronounced workfunction-gradient driving charge separation and transport.

On the PbX_2 –PbS side of the EDT–PbS interface, however, the behavior of the SCE is unexpected, dropping by more than 30% in a 100 nm wide region. We explain this sharp drop in SCE near the interface via the schematic band alignment proposed in Figure 3c,d, which occurs if $\Phi_{\text{EDT}} < \Phi_{\text{PbX}_2}$. In this case, band-bending at the interface results in a small drift component that is opposed to the desired direction of carrier flow. While photogenerated holes can diffuse through the short distance that separates them from the shallow EDT–PbS valence band, photogenerated electrons are subject to a much reduced driving force and are lost to recombination before reaching the ETL. Forward-bias exacerbates the effect by enhancing the undesired band-bending. This discrepancy between the previously proposed smooth band alignment,^[13] expected from ultraviolet photoelectron spectroscopy (UPS), and this one, suggested by the SCE, could arise from the fact that UPS is measured under

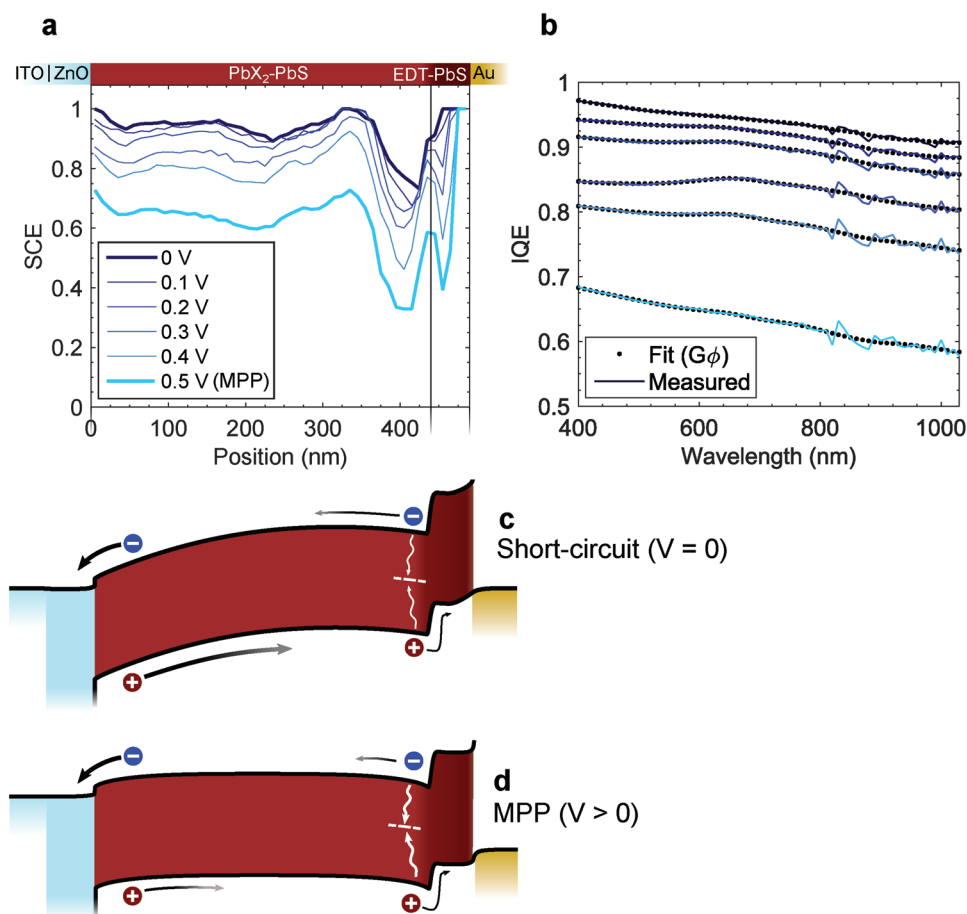


Figure 3. Calculating $\phi(z)$: spatial collection efficiency in CQD solar cells reveals local imperfections. a) Calculated SCE as function of bias voltage for $r = 2000$. b) Calculated IQE (lines), found by multiplying G and the SCE ϕ , showing a good fit with the experimental data (points). c,d) Schematic of the proposed operando band alignment at short-circuit and maximum-power point. When photogenerated near the PbX₂-PbS:EDT-PbS interface, few electrons can travel to the electron-accepting contact due to unfavorable band-bending, while photogenerated holes have a higher chance of diffusing toward the hole-accepting contact due to the workfunction gradient. Under forward-bias, the bands flatten throughout the active layer, reducing the drift-component in carrier transport.

high vacuum, whereas devices are fabricated in air and operate in N₂ at atmospheric pressure, conditions which are known to have an impact on the position of the energy bands of PbS CQDs, especially in the EDT-treated HTL.^[36] A solution to this issue would be to increase the p-doping density in the EDT-PbS layer or to make the PbX₂-PbS workfunction shallower, although the latter might have a negative impact on the band alignment at the ZnO heterojunction.

We further analyze the results by multiplying the SCEs and the generation profile of Figure 1e to obtain the bias-dependent photocurrent contribution profiles of **Figure 4a**. For instance, we observe that imperfections at the rear interface have a much lower impact on the total current than imperfections at the front interface. This is not, however, an indication that the rear-interface has only a limited impact on device performance, as advances in this region have previously led to improvements in V_{OC} and FF.^[13] Integrating the photocurrent profiles over the position z yields the cumulative photocurrent shown in Figure 4b. This visualization further illustrates the respective contributions to the total photocurrent from each region of the active layer, showing, for instance, that half of J_{SC} originates

from the first 125 nm of material only and that the EDT layer contributes less than 2 mA cm⁻². In addition, Figure 4b renders explicit the separation of optical and charge carrier transport losses with respect to the detailed-balance limit for J_{SC} and J_{MPP} .^[37] We observe that, at the current optimal active layer thickness, losses totaling 15 mA cm⁻² are closely split between optical (46%) and carrier transport (54%) losses, in line with the mitigation of the absorption-extraction compromise through active-layer thickness optimization in best-performing CQD cells.^[32] These results allow us to reassert that optical considerations are as important as materials improvement to enhance the photocurrent and fill factor of CQD solar cells.

We note that the method is more widely applicable in thin-film solar cell architectures. As opposed to analytical methods, regularization-based methods such as the one presented herein work even when single-pass light absorption is far from complete, a situation common to most perovskite, organics, and CQD devices. In addition, the Gaussian-noise regularization scheme allows one to resolve sharp features in SCE profiles arising from surface recombination, interfacial defects, or heterojunctions, making it promising in the study of the

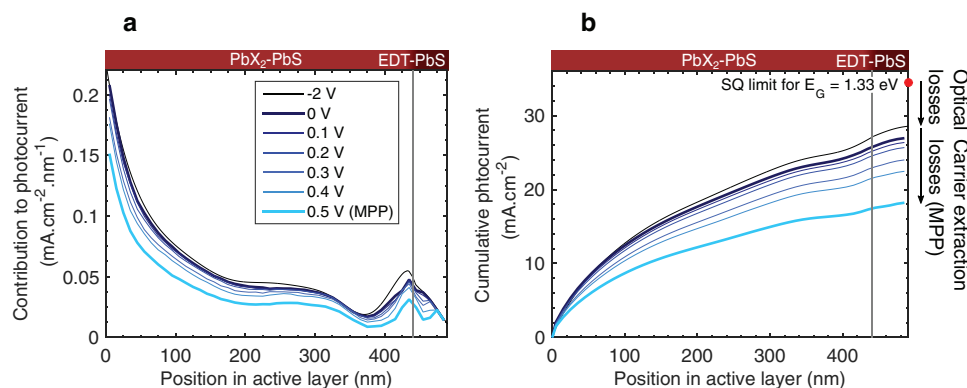


Figure 4. Identifying optical and carrier extraction losses. a) Contribution to photocurrent profiles obtained by multiplying the SCEs with the photogeneration rate shown in Figure 1e. b) Cumulative J_{SC} as function of depth, with optical and recombination losses identified. The Shockley–Queisser limit value at the bandgap corresponding to the exciton peak (1.33 eV) is also shown.

degradation of perovskite active layers near their electron- and hole-transport layers^[38,39] or CQD-organic hybrid devices,^[40,41] for instance.

In sum, we used a Gaussian-noise regularized least-squares approach to calculate numerically the spatial collection efficiency in CQD solar cells. This method provides a systematic approach for computing physically realistic solutions and removes the need for free parameters. From the SCE profiles, we deduce that CQD devices are not fully depleted at zero applied bias, and we confirm that the ZnO:PbS heterojunction is the most important component for charge extraction. We also observe that the HTL does not fulfill its intended role of providing a back-surface field, since it does not deplete the active layer, but instead negatively impacts SCE at the interface. We decompose photocurrent losses into their optical and recombination components, noting that efforts are still needed on both fronts to improve J_{SC} and FF in these photovoltaic devices. The method could be further improved by increasing the EQE input data resolution and refining the optical model to improve the fit with experimental absorption spectra. The method for the determination of the SCE is readily generalizable to other thin-film architectures and provides a tool to probe the efficiency of solar cells through the depth of their active layer.

4. Experimental Section

CQD Synthesis and Ligand Exchange: The synthetic protocol previously reported by Hines and Scholes was followed.^[42] Ligand exchange from oleic acid to lead halides (PbI_2 and $PbBr_2$) was carried out in solution following the previous report^[32] with a redispersion concentration of 325 mg mL^{-1} in butylamine. Ligand exchange from oleic acid to EDT was performed following the protocol in ref. [5].

Solar Cell Fabrication: Indium tin oxide (ITO) substrates on glass (Delta Technologies, $5\text{--}15 \text{ } \Omega \text{sq}^{-1}$) were cleaned with sequential detergent (Triton X-100), acetone, and isopropanol ultrasonic baths for 15 min each. Two layers of ZnO nanoparticles^[13] were spin-coated at a spin speed of 3000 rpm for 30 s. CQD films were deposited by spin-coating at 2500 rpm and annealed in an oven in a N_2 glovebox at 70°C for 10 min. Devices were then left to dry for 24 h in air. 120 nm of gold was thermally evaporated by e-beam in an Angstrom Engineering Åmod deposition system in an Innovative Technology N_2 glovebox.

AM1.5 Photovoltaic Performance Characterization: Devices were kept in an inert N_2 atmosphere. Illumination was performed with a Scientech SF150 solar simulator, calibrated for 1 sun total irradiance with an NIST-traceable silicon reference cell. Current–voltage characteristics were obtained with a Keithley 2400 source measure unit (SMU).

External Quantum Efficiency: EQE was measured using a Newport QUANTX-300 system. Monochromatic light excitation was mechanically chopped at a frequency of 25 Hz. The device was kept in an inert N_2 atmosphere. The device was light-biased with continuous white light illumination from a Newport IQE-LIGHT-BIAS source.^[24,25]

Spectroscopic Ellipsometry: Spectroscopic ellipsometry was performed using a Horiba UVISSEL Plus Extended Range ellipsometer with a 200 ms integration time, a 5 nm step size, and a 1 mm diameter spot size at an incident angle of 70° . Soda-lime glass slides were used as substrates for each individual material, with their back covered with cloudy adhesive tape to ensure back-reflections were diffusively reflected away from the detector. Fitting was performed using Horiba's DeltaPsi2 dedicated software. Fitting procedure and further details are available in the Supporting Information.

Transfer Matrix Calculations: TM calculations were performed using an open-source MATLAB code developed by the McGehee group at Stanford University.^[27]

Numerical Solver: The convex program (S.7) was solved on MATLAB using the CVX package^[43,44] with the SeDuMi^[45] solver.

Supporting Information

Supporting Information is available from the Wiley Online Library or from the author.

Acknowledgements

The authors thank L. Levina, E. Palmiano, D. Kopilovic, and R. Wolowicz for technical support throughout the project. The authors also thank M. Biondi and M.-J. Choi for help with device fabrication and J. Z. Fan, P. Todorović, R. Quintero-Bermudez, and G. Walters for fruitful discussions. SEM imaging was performed at the Ontario Centre for the Characterization of Advanced Materials (OCCAM, Toronto, ON). This project was financially supported by the Natural Sciences and Engineering Research Council of Canada (NSERC). O.O. received financial support through an NSERC Canada Graduate Scholarship. A.L.-L. received financial support through a Doctoral Research Scholarship from the Fonds de recherche du Québec - Nature et technologies (FRQNT).

Conflict of Interest

The authors declare no conflict of interest.

Keywords

colloidal quantum dots, Gaussian regularization least-squares, photovoltaics, spatial collection efficiency

Received: October 3, 2019

Published online:

-
- [1] A. P. Alivisatos, *Science* **1996**, *271*, 5251.
- [2] P. V. Kamat, *J. Phys. Chem. C* **2008**, *112*, 48.
- [3] M. V. Kovalenko, *Nat. Nanotechnol.* **2015**, *10*, 12.
- [4] E. M. Sanehira, A. R. Marshall, J. A. Christians, S. P. Harvey, P. N. Ciesielski, L. M. Wheeler, P. Schulz, L. Y. Lin, M. C. Beard, J. M. Luther, *Sci. Adv.* **2017**, *3*, 10.
- [5] J. Xu, O. Voznyy, M. Liu, A. R. Kirmani, G. Walters, R. Munir, M. Abdelsamie, A. H. Proppe, A. Sarkar, F. P. G. de Arquer, M. Wei, B. Sun, M. Liu, O. Ouellette, R. Quintero-Bermudez, J. Li, J. Fan, L. Quan, P. Todorović, H. Tan, S. Hoogland, S. O. Kelley, M. Stefić, A. Amassian, E. H. Sargent, *Nat. Nanotechnol.* **2018**, *13*, 456.
- [6] A. Polman, M. Knight, E. C. Garnett, B. Ehrler, W. C. Sinke, *Science* **2016**, *352*, 6283.
- [7] S. Volk, N. Yazdani, E. Sanusoglu, O. Yarema, M. Yarema, V. Wood, *J. Phys. Chem. Lett.* **2018**, *9*, 6.
- [8] S. Kahmann, M. Sytnyk, N. Schrenker, G. J. Matt, E. Spiecker, W. Heiss, C. J. Brabec, M. A. Loi, *Adv. Electron. Mater.* **2018**, *4*, 1700348.
- [9] J. Jean, T. S. Mahony, D. Bozyigit, M. Sponseller, J. Holovsky, M. G. Bawendi, V. Bulović, *ACS Energy Lett.* **2017**, *2*, 11.
- [10] O. Voznyy, L. Levina, F. Fan, G. Walters, J. Z. Fan, A. Kiani, A. H. Ip, S. M. Thon, A. H. Proppe, M. Liu, E. H. Sargent, *Nano Lett.* **2017**, *17*, 12.
- [11] Y. Liu, D. Kim, O. P. Morris, D. Zhitomirsky, J. C. Grossman, *ACS Nano* **2018**, *12*, 3.
- [12] J. Choi, Y. Kim, J. W. Jo, J. Kim, B. Sun, G. Walters, F. P. García de Arquer, R. Quintero-Bermudez, Y. Li, C. S. Tan, L. Quan, A. P. T. Kam, S. Hoogland, Z. Lu, O. Voznyy, E. H. Sargent, *Adv. Mater.* **2017**, *29*, 33.
- [13] C.-H. M. Chuang, P. R. Brown, V. Bulović, M. G. Bawendi, *Nat. Mater.* **2014**, *13*, 8.
- [14] D. Zhitomirsky, O. Voznyy, L. Levina, S. Hoogland, K. W. Kemp, A. H. Ip, S. M. Thon, E. H. Sargent, *Nat. Commun.* **2014**, *5*, 3803.
- [15] J. Sinkkonen, J. Ruokolainen, P. Uotila, A. Hovinen, *Appl. Phys. Lett.* **1995**, *66*, 2.
- [16] G. Segev, H. Dotan, D. S. Ellis, Y. Piekner, D. Klotz, J. W. Beeman, J. K. Cooper, D. A. Grave, I. D. Sharp, A. Rothschild, *Joule* **2018**, *2*, 210.
- [17] X. Liu, J. Sites, *J. Appl. Phys.* **1994**, *75*, 577.
- [18] Y. Pang, H. Efstathiadis, D. Dwyer, M. Eisaman, in *2015 IEEE 42nd Photovoltaic Specialist Conf. (PVSC)*, IEEE, Piscataway, NJ **2015**.
- [19] E. Tuominen, M. Acerbis, A. Hovinen, T. Siirtola, J. Sinkkonen, *Phys. Scr.* **1997**, *1997*, T69.
- [20] P. H. Rekemeyer, C.-H. M. Chuang, M. G. Bawendi, S. Gradecak, *Nano Lett.* **2017**, *17*, 10.
- [21] H. Leamy, *J. Appl. Phys.* **1982**, *53*, 6.
- [22] J. Choi, J. W. Jo, F. P. G. de Arquer, Y.-B. Zhao, B. Sun, J. Kim, M.-J. Choi, S.-W. Baek, A. H. Proppe, A. Seifitokaldani, D.-H. Nam, P. Li, O. Ouellette, Y. Kim, O. Voznyy, S. Hoogland, S. O. Kelley, Z. H. Lu, E. H. Sargent, *Adv. Mater.* **2018**, *30*, 29.
- [23] Q. Lin, A. Armin, R. C. R. Nagiri, P. L. Burn, P. Meredith, *Nat. Photonics* **2015**, *9*, 2.
- [24] D. Abou-Ras, T. Kirchartz, U. Rau, *Advanced Characterization Techniques for Thin Film Solar Cells*, John Wiley & Sons, New York **2016**.
- [25] Standard test method for spectral responsivity measurements of photovoltaic devices, Technical Report, ASTM International **2015**.
- [26] M. Law, M. C. Beard, S. Choi, J. M. Luther, M. C. Hanna, A. J. Nozik, *Nano Lett.* **2008**, *8*, 11.
- [27] G. F. Burkhard, E. T. Hoke, M. D. McGehee, *Adv. Mater.* **2010**, *22*, 30.
- [28] C. Donolato, *Inverse Probl.* **1986**, *2*, 3.
- [29] C. Donolato, *J. Appl. Phys.* **2001**, *89*, 10.
- [30] P. C. Hansen, *BIT Numer. Math.* **1990**, *30*, 4.
- [31] C. M. Bishop, *Neural Comput.* **1995**, *7*, 108.
- [32] M. Liu, O. Voznyy, R. Sabatini, F. P. G. de Arquer, R. Munir, A. H. Balawi, X. Lan, F. Fan, G. Walters, A. R. Kirmani, S. Hoogland, F. Laquai, A. Amassian, E. H. Sargent, *Nat. Mater.* **2017**, *16*, 2.
- [33] K. Kemp, C. Wong, S. Hoogland, E. Sargent, *Appl. Phys. Lett.* **2013**, *103*, 21.
- [34] J. Nelson, *The Physics of Solar Cells*, Imperial College Press, London, UK **2003**, Ch. 8.
- [35] A. H. Proppe, J. Xu, R. P. Sabatini, J. Z. Fan, B. Sun, S. Hoogland, S. O. Kelley, O. Voznyy, E. H. Sargent, *Nano Lett.* **2018**, *18*, 11.
- [36] A. R. Kirmani, A. D. Sheikh, M. R. Niazi, M. A. Haque, M. Liu, F. P. G. de Arquer, J. Xu, B. Sun, O. Voznyy, N. Gasparini, D. Baran, T. Wu, E. H. Sargent, A. Amassian, *Adv. Mater.* **2018**, *30*, 35.
- [37] W. Shockley, H. J. Queisser, *J. Appl. Phys.* **1961**, *32*, 510.
- [38] A. Guerrero, J. You, C. Aranda, Y. S. Kang, G. Garcia-Belmonte, H. Zhou, J. Bisquert, Y. Yang, *ACS Nano* **2015**, *10*, 218.
- [39] T. A. Berhe, W.-N. Su, C.-H. Chen, C.-J. Pan, J.-H. Cheng, H.-M. Chen, M.-C. Tsai, L.-Y. Chen, A. A. Dubale, B.-J. Hwang, *Energy Environ. Sci.* **2016**, *9*, 323.
- [40] S.-W. Baek, S.-H. Lee, J. H. Song, C. Kim, Y.-S. Ha, H. Shin, H. Kim, S. Jeong, J.-Y. Lee, *Energy Environ. Sci.* **2018**, *11*, 8.
- [41] H. Aqoma, M. A. Mubarak, W. Lee, W. T. Hadmojo, C. Park, T. K. Ahn, D. Y. Ryu, S.-Y. Jang, *Adv. Energy Mater.* **2018**, *8*, 23.
- [42] M. A. Hines, G. D. Scholes, *Adv. Mater.* **2003**, *15*, 21.
- [43] M. Grant, S. Boyd, CVX: Matlab software for disciplined convex programming, version 2.1, <http://cvxr.com/cvx> (accessed: May 2019).
- [44] M. Grant, S. Boyd, in *Recent Advances in Learning and Control* (Eds: V. Blondel, S. Boyd, H. Kimura), Lecture Notes in Control and Information Sciences, Vol. 371, Springer-Verlag Limited, Berlin **2008**.
- [45] J. F. Sturm, *Optim. Method. Softw.* **1999**, *11*, 625.